molecules

MDPI

Article

In Situ Encapsulation of Graphene Quantum Dots in Highly Stable Porphyrin Metal-Organic Frameworks for Efficient Photocatalytic CO_2 Reduction

Qin Yu [1,†], Xusheng Wang [1,2,3,4,*,†], Wenbin Wu [1], Xinya Feng [1], Deyu Kong [1], Usman Khan [1], Xiaohui Ren [5] and Lan Li [6]

1 Institute of Functional Porous Materials, School of Materials Science and Engineering, Zhejiang Sci-Tech University, Hangzhou 310018, China; 2021316101103@mails.zstu.edu.cn (Q.Y.); 2022316101108@mails.zstu.edu.cn (W.W.); 2022316101030@mails.zstu.edu.cn (X.F.); 2022316101070@mails.zstu.edu.cn (D.K.); usman@zstu.edu.cn (U.K.)
2 Guangdong Provincial Key Laboratory of Functional Supramolecular Coordination Materials and Applications, Jinan University, Guangzhou 510632, China
3 Tongxiang Research Institute, Zhejiang Sci-Tech University, Jiaxing 314500, China
4 Zhejiang LINIX Motor Co., Ltd., Jinhua 322118, China
5 The State Key Laboratory of Refractories and Metallurgy, School of Materials and Metallurgy, Wuhan University of Science and Technology, Wuhan 430081, China; xhren@wust.edu.cn
6 College of Materials and Chemistry, China Jiliang University, Hangzhou 310018, China; lanli@cjlu.edu.cn
* Correspondence: xswang@zstu.edu.cn
† These authors contributed equally to this work.

Abstract: Photocatalytic CO_2 reduction to valuable hydrocarbon solar fuel is of great significance but still challenging. Strong CO_2 enrichment ability and easily adjustable structures make metal-organic frameworks (MOFs) potential photocatalysts for CO_2 conversion. Even though pure MOFs have the potential for photoreduction of CO_2, the efficiency is still quite low due to rapid photogenerated electron–hole recombination and other drawbacks. In this work, graphene quantum dots (GQDs) were in situ encapsulated into highly stable MOFs via a solvothermal method for this challenging task. The GQDs@PCN-222 with encapsulated GQDs showed similar Powder X-ray Diffraction (PXRD) patterns to PCN-222, indicating the retained structure. The porous structure was also retained with a Brunauer–Emmett–Teller (BET) surface area of 2066 m^2/g. After incorporation of GQDs, the shape of GQDs@PCN-222 particles remained, as revealed by the scanning electron microscope (SEM). As most of the GQDs were covered by thick PCN-222, it was hard to observe those GQDs using a transmission electron microscope (TEM) and a high-resolution transmission electron microscope (HRTEM) directly, the treatment of digested GQDs@PCN-222 particles by immersion in a 1 mM aqueous KOH solution can make the incorporated GQDs visible in TEM and HRTEM. The linker, deep purple porphyrins, make MOFs a highly visible light harvester up to 800 nm. The introduction of GQDs inside PCN-222 can effectively promote the spatial separation of the photogenerated electron–hole pairs during the photocatalytic process, which was proved by the transient photocurrent plot and photoluminescence emission spectra. Compared with pure PCN-222, the obtained GQDs@PCN-222 displayed dramatically enhanced CO production derived from CO_2 photoreduction with 147.8 μmol/g/h in a 10 h period under visible light irradiation with triethanolamine (TEOA) as a sacrificial agent. This study demonstrated that the combination of GQDs and high light absorption MOFs provides a new platform for photocatalytic CO_2 reduction.

Keywords: metal-organic frameworks; porous materials; graphene quantum dots; photocatalyst; photocatalysis; photoreduction; CO_2; PCN-222; porphyrin; MOFs

check for updates

Citation: Yu, Q.; Wang, X.; Wu, W.; Feng, X.; Kong, D.; Khan, U.; Ren, X.; Li, L. In Situ Encapsulation of Graphene Quantum Dots in Highly Stable Porphyrin Metal-Organic Frameworks for Efficient Photocatalytic CO_2 Reduction. *Molecules* **2023**, *28*, 4703. https://doi.org/10.3390/molecules28124703

Academic Editor: Igor Djerdj

Received: 18 May 2023
Revised: 1 June 2023
Accepted: 10 June 2023
Published: 12 June 2023

Copyright: © 2023 by the authors. Licensee MDPI, Basel, Switzerland. This article is an open access article distributed under the terms and conditions of the Creative Commons Attribution (CC BY) license (https://creativecommons.org/licenses/by/4.0/).

1. Introduction

The excessive emission of CO_2 is the major contributor to global warming [1–3]. Capture and conversion of CO_2 to value-added chemicals is a major issue for scientists all around the world [4–6]. Photocatalysis is an energy-saving and highly efficient technology [7–17]. As a kind of photocatalytic technology, photocatalytic reduction of CO_2 to valuable chemicals is of great significance but still challenging [18–22]. So far, several photocatalysts have been devoted to photocatalytic CO_2 reduction, but are still unsatisfied due to low adsorption of CO_2, narrow and weak light absorption, and rapid recombination of the photogenerated electron–hole pairs [6,23,24]. Searching new kinds of photocatalysts for photocatalytic CO_2 reduction under visible light region is still vital and challenging work.

Metal-organic frameworks (MOFs), assembled by inorganic metal ions or clusters and organic ligands through coordination bonds, are a new kind of material with high porosity, high specific surface area, and easily adjustable structures [25–30]. With those excellent properties, MOFs had been widely used in many fields, such as gas adsorption and separation, drug loading, catalysis and so on [31–38]. Especially, strong CO_2 enrichment ability makes MOFs to be potential photocatalysts for CO_2 conversion [39]. In addition, the photocatalytic conversion of CO_2 by MOFs can be promoted by adjusting the catalytic active center, light absorption range and energy bandgap position, etc. [40–42]. Benefitting from those advantages, MOFs had been studied for the photocatalytic conversion of CO_2 directly [43–48]. For example, NH_2-MIL-125(Ti) had been used for photoreduction of CO_2 under visible light irradiation by the Li group, with produced formic acid reaching 16 μmol/g/h [47]. Afterwards, with highly visible light harvesting ability, porphyrin-involved MOFs, PCN-222, had also been applied for selective capture and further photoreduction of CO_2, with activity reaching 60 μmol/g/h [48]. Even though pure MOFs have the potential for photoreduction of CO_2, the efficiency is still quite low due to rapid photogenerated electron–hole recombination and other drawbacks. To solve those problems, components, such as platinum, gold, silver, C_3N_4, graphene, and Zn_2GeO_4, had been combined with MOFs to improve the photocatalytic efficiency, but it is still hard to satisfy the high requirements [49–53].

Recently, graphene quantum dots (GQDs) became a rising star in carbon nanomaterials due to their excellent light stability, biocompatibility, water solubility and low toxicity [54]. The diameter of GQDs is often less than 10 nm, mainly composed of sp^2 amorphous carbon and sp^2 graphite carbon. In particular, the GQDs can absorb light from ultraviolet to near-infrared, and have good luminescence and electron conduction ability. In addition, the GQDs can be used as electronic sinks, making them potential photocatalytic cocatalysts. For example, Kang et al. reported GQDs can be combined with carbon nitride to form graphene quantum dots–carbon nitride nanocomposite for photocatalytic solar water splitting with overall solar energy conversion efficiency of 2.0% [55].

In order to solve the problem of low activity of photocatalytic reduction of CO_2 by pure MOFs, herein, GQDs had been in situ encapsulated into a highly stable porphyrin MOF, PCN-222, obtaining GQDs@PCN-222. The GQDs@PCN-222 can combine the advantages of MOFs and GQDs, overcome the disadvantage of low catalytic activity of pure MOFs, and be used for high-efficiency photocatalytic CO_2 reduction.

2. Results and Discussion

2.1. Synthesis and Characterization of GQDs

GQDs were prepared by electrolysis of graphite electrodes following the reported method [55,56]. Typically, 500 mL of deionized water was added into an 800 mL beaker and two high-purity graphite electrodes were put into the above beaker. The distance between the two electrodes was 7 cm in the beaker, and the potential was set as 30 V DC. The beaker was covered by a plastic film to prevent the evaporation of water and the contamination of dust during the electrolysis process. Noting that hydrogen and oxygen gas will be produced during the electrolysis process, some small holes should be punched on the cover. For safety, the equipment should be placed into a fume hood in case of the accumulation

of explosive hydrogen. The clear and colorless water gradually turned black during the two weeks of electrolysis. Afterwards, the black electrolyte was centrifuged for one hour with a speed of 20,000 rpm to remove the large particles, and the supernatant was then evaporated to obtain the desired GQDs.

The transmission electron microscope (TEM) and the high-resolution transmission electron microscope (HRTEM) gave a visual method to measure the size and morphology of GQDs. As shown in Figure 1a,b pictured by TEM, ultrafine GQDs were obtained with a size of around 3 nm and the size distributions were quite uniform. HRTEM (Figure 1c) further discovered that the GQDs with high crystallinity and a 0.207 nm lattice spacing of graphene (101) are identified. The atomic force microscope (AFM) is an effective piece of equipment to measure the thickness of GQDs. As shown in Figure 1d,e, the thickness of the prepared GQDs was about 2.0 nm and the corresponding layer number is about 5. Interestingly, a small amount of GQDs can even reach a single layer, and the thickness is only about 0.34 nm. The photoluminescence (PL) emission properties of GQDs were further studied with a fluorescence spectrometer. The PL emission spectra showed a typical excitation-wavelength dependent behavior of GQDs: shifting the excitation wavelength from λ = 300 to 500 nm, the corresponding maximum of emission spectra are shifted from λ = 466 to 577 nm (Figure 1f). This phenomenon is similar to the previously reported results [55,56]. While the PL emission in GQDs is not well understood, the prevailing view is that emission results from radiative recombination at surface confined defect states. The excitation-wavelength-dependent behavior is thought to be due to the heterogeneity of such emission states in the sample from either multiple emission sites on each dot or different emissive sites between individual dots.

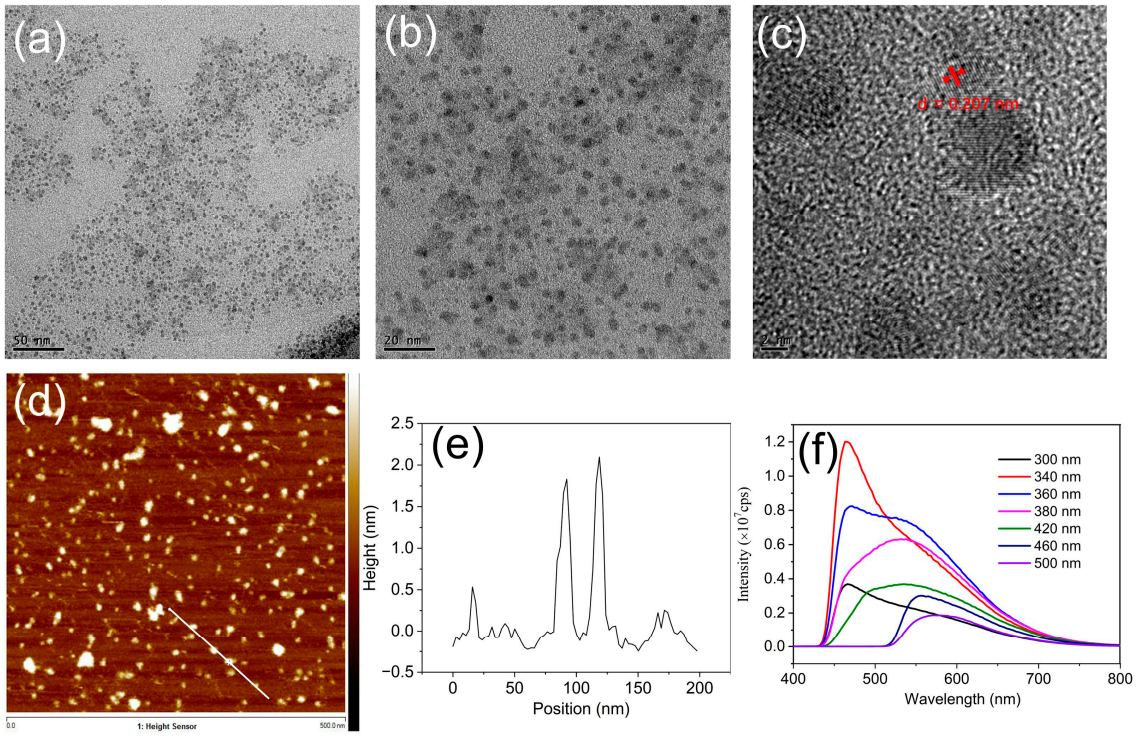


Figure 1. Characterizations of GQDs prepared by electrolysis of graphite electrodes. (**a**,**b**) TEM and (**c**) HRTEM of GQDs with a scale bar of 50 nm, 20 nm, and 2 nm, respectively; (**d**) AFM of GQDs; (**e**) The height of selected GQDs in (**d**); (**f**) PL emission spectra of GQDs aqueous dispersion at different excitation wavelengths (300 nm to 500 nm).

2.2. Synthesis and Characterization of PCN-222 and GQDs@PCN-222

The synthesis and activation of pure PCN-222 followed the reported literature [48]. The successful synthesis of PCN-222 was proved by Powder X-Ray Diffraction (PXRD), which

showed almost identical patterns to the simulated one (Figure 2a). N_2 sorption isotherm is an effective way to characterize the porous structure of photocatalysts. As shown in Figure 2b, both PCN-222 have a completely reversible Type IVb isotherm according to the classifications of IUPAC, which indicates that mesopores with pore width lower than 4 nm are existing [57]. The pore size distribution of PCN-222 showed that the biggest pore width of PCN-222 is around 3.7 nm (Figure S1), which is similar to the previously reported results. The average pore size of PCN-222 is around 2.3 nm. In addition, a really high Brunauer–Emmett–Teller (BET) surface area of 2339 m^2/g was also obtained by the N_2 sorption isotherm (Figure 2b). As the size of GQDs is smaller than the pore of PCN-222, those GQDs might be enclosed within the framework pores of PCN-222. The GQDs were in situ encapsulated into the MOFs by solvothermal method to obtain GQDs@PCN-222. The GQDs@PCN-222 with encapsulated GQDs showed similar PXRD patterns to PCN-222, indicating the retained crystal structure. The porous structure was also retained with a high BET surface area of 2066 m^2/g. Notably, the pore size distribution of GQDs@PCN-222 had no obvious difference from PCN-222 with the biggest pore width of around 3.7 nm. The average pore size of GQDs@PCN-222 is also similar to PCN-222 with a value of 2.3 nm.

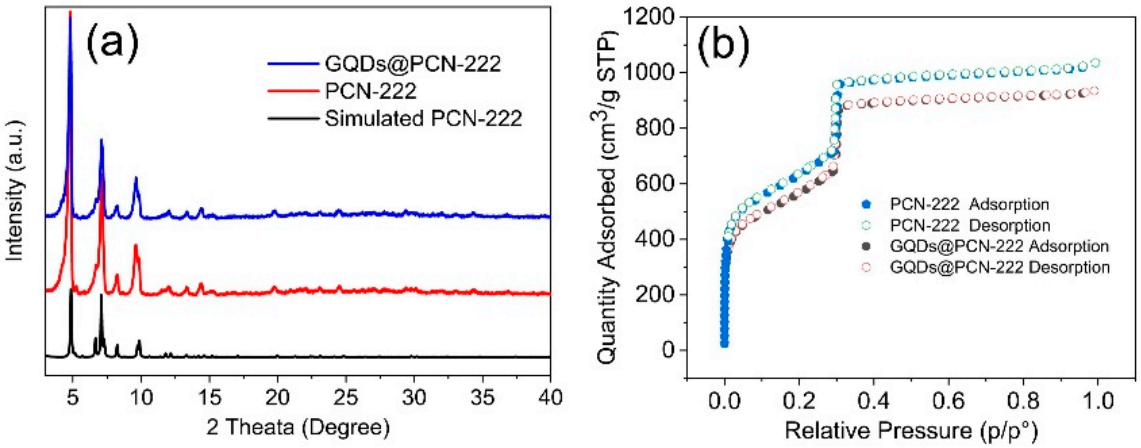


Figure 2. Structural characterization of PCN-222 and GQDs@PCN-222. (**a**) PXRD patterns of simulated PCN-222, PCN-222, and GQDs@PCN-222; (**b**) N_2 sorption isotherms of PCN-222, and GQDs@PCN-222.

The scanning electron microscope (SEM) images showed that all the pure PCN-222 particles had a nanorod shape and a diameter of around 500 nm (Figure S2). After the incorporation of GQDs, the shape of GQDs@PCN-222 rods was retained but the diameter was reduced to 150 nm (Figure 3a–c). The decreased diameter of MOFs might be ascribed to the existence of carboxylate groups on the surface of incorporated GQDs. As most of the GQDs were covered by thick PCN-222, it was hard to observe those GQDs using high-resolution transmission electron microscopy (HRTEM) directly (Figure 3d–f) [58]. Comparatively, GQDs can be observed on the surface of GQDs/PCN-222 as GQDs were not covered by MOFs (Figure S3). For the more thorough characterization of the GQDs particles incorporated in GQDs@PCN-222 rods, the MOF composite sample was digested by immersing it in a 1 mM aqueous KOH solution. This treatment resulted in the dissolution of the GQDs@PCN-222 rods to yield a suspension of the GQDs because PCN-222 is not stable while GQDs are stable in the high alkali condition. GQDs were then obtained by filtration and extraction of the suspension of the GQDs with diethyl ether. HRTEM of these GQDs (Figure 3g–i) revealed an average size of the GQDs of approximately 3 nm, with a rather narrow size distribution.

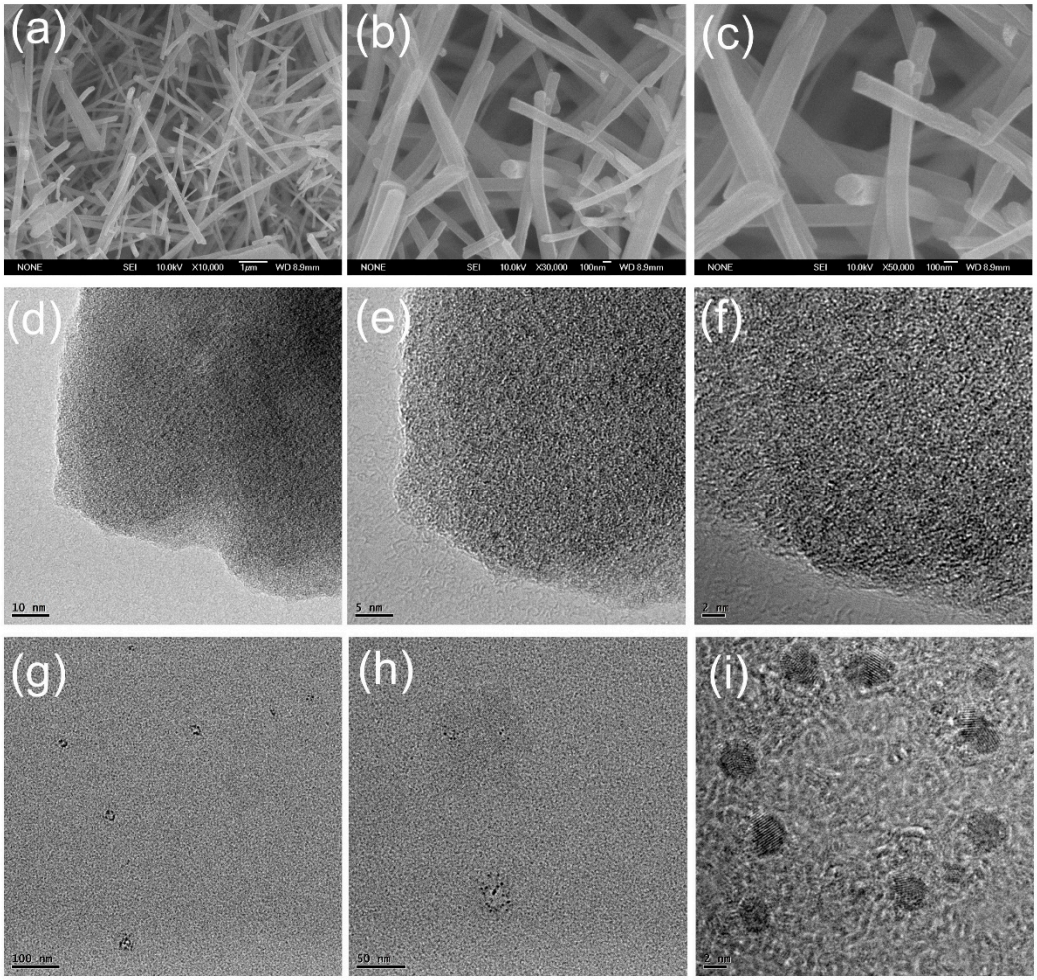


Figure 3. Electron microscope images of GQDs@PCN-222, and the digested GQDs@PCN-222. (**a**–**c**) SEM images of GQDs@PCN-222 with a scale bar of 1 μm, 100 nm, 100 nm, respectively; (**d**–**f**) TEM and HRTEM images of GQDs@PCN-222 with a scale bar of 10 nm, 5 nm, 2 nm, respectively; (**g**–**i**) TEM and HRTEM images of the digested GQDs@PCN-222 by KOH solution with a scale bar of 100 nm, 50 nm, 2 nm, respectively.

2.3. Photocatalytic Properties

The solid UV-Vis diffuse reflectance spectrum (UV-Vis DRS) showed that the absorption range of organic ligand meso-tetra(4-carboxyphenyl)porphine (H_2TCPP) can reach up to 800 nm with peaks of Soret band at 355 nm and Q bands at 514, 553, 591, and 646 nm (Figure S4a). Correspondingly, a similar light absorption range and peaks (Soret band at 449 nm and Q bands at 520, 560, 595, and 652 nm) were obtained for PCN-222 synthesized by a solvothermal method involving H_2TCPP (Figure S5a). Notably, after the encapsulation of GQDs in MOFs, no obvious change of absorption peaks (Soret band at 451 nm and Q bands at 525, 562, 596, 654 nm) and light harvesting range can be detected (Figure 4a). Even though the absorbance range and peaks of GQDs@PCN-222 did not change much after encapsulation of GQDs, the photocurrent had increased significantly (Figure 4d), and the PL emission intensity decreased obviously (Figure 4e), which indicated that the introduction of GQDs improves the separation efficiency and decreases the recombination of photogenerated electron–hole pairs of the catalyst. The bandgap of ligand H_2TCPP was calculated from the Tauc plot to be 1.75 eV (Figure S4b), while the bandgaps of PCN-222 and GQDs@PCN-222 were calculated to be 1.79 eV and 1.82 eV, respectively (Figure 4b and Figure S5b) [59,60]. The above results indicated that H_2TCPP, PCN-222, and GQDs@PCN-222 have similar values of bandgap. The conduction band (CB) minimums of PCN-222 and GQDs@PCN-222 were also measured by Mott–Schottky curves to be −0.9 eV

and −0.95 eV, respectively (Figure 4c and Figure S6). Accordingly, the valence band (VB) maximums of PCN-222 and GQDs@PCN-222 were calculated to be 0.89 eV and 0.87 eV, respectively. Therefore, both PCN-222 and GQDs@PCN-222 are thermodynamics favorable for photocatalytic CO_2 reduction with triethanolamine (TEOA) as a sacrificial agent.

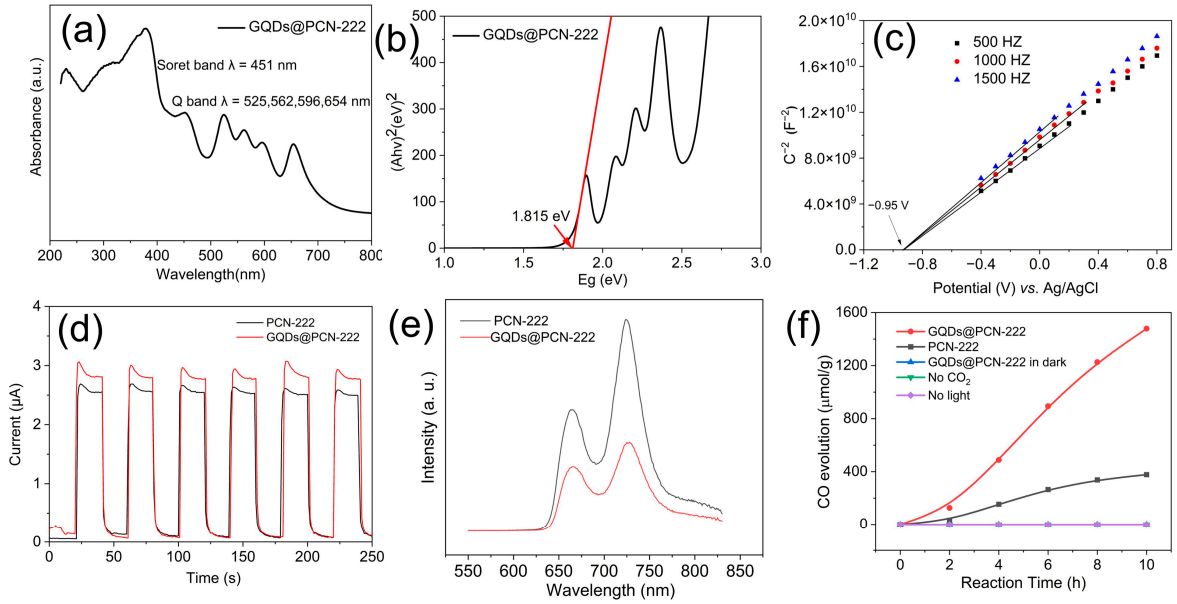


Figure 4. Photocatalytic performance and the photocatalytic mechanism-related characterizations. (**a**) Solid UV-vis diffuse reflectance spectrum of GQDs@PCN-222; (**b**) Tauc plot of GQDs@PCN-222; (**c**) Mott-Schottky plots of GQDs@PCN-222 with a frequency of 500, 1000, and 1500 HZ; (**d**) Photocurrent and (**e**) PL emission with excitation wavelength at 365 nm of PCN-222 and GQDs@PCN-222; (**f**) Photocatalytic CO_2 reduction by photocatalysts.

In view of the advantages of GQDs@PCN-222 rods, it was then used for visible light photocatalytic CO_2 reduction. GQDs@PCN-222 rods were evenly dispersed on the quartz filter membrane, which had been placed in the solid-gas photocatalytic reaction device. A mixture of acetonitrile and triethanolamine (the volume ratio of acetonitrile to TEOA is 4:1) was then added into the photocatalytic reaction device, too. After three instances of vacuuming and CO_2 filling (making sure that all the air in the system was replaced by CO_2), the reaction system was balanced in dark for 1 h and then the photoreduction reaction of CO_2 started after visible light irradiation (300 W Xe lamp with 420 nm cut-off filter). The product was measured by gas chromatography with both TCD and FID detectors every 2 h. As shown in Figure 4f, the produced CO of GQDs@PCN-222 increased steadily under visible light irradiation, and its activity reached 1 500 μmol/g after 10 h. No hydrogen gas was detected during the whole photocatalytic process. Relative to the PCN-222 (380 μmol/g), the activity of GQDs@PCN-222 increased nearly four times. At the same time, the comparative experiment showed that no CO was produced without GQDs@PCN-222. In addition, it has no catalytic activity when there is no CO_2 or light. Combined with the above photocurrent and PL emission data, we speculate that the introduction of GQDs can greatly improve the separation of photogenerated carriers of PCN-222, and then improve the visible light photocatalytic carbon dioxide reduction activity. The enhanced activity of GQDs@PCN-222 than PCN-222 is because the GQDs can be used as an electronic sink, making them potential photocatalytic cocatalysts to accumulate the photogenerated electrons from PCN-222. A comparison of photocatalysts for CO_2 reduction with previous works had also been summarized in Table S1, which showed that GQDs@PCN-222 is an outstanding photocatalyst for CO_2 reduction. The proposed photocatalytic reduction mechanism of CO_2 to CO by GQDs@PCN-222 can be illustrated as follows (Figure 5). Under visible light irradiation, photogenerated electrons

were hopped from VB to CB of PCN-222 and then transferred to GQDs covered by MOF. The electrons will be accumulated on GQDs and reduce the adsorbed CO_2 to CO. The residual holes on PCN-222 will oxidize the organic amine (TEOA) to oxidized organic amine. The overall reduction process of CO_2 in the form of photochemical reactions was also shown (Equations (1)–(3)). Powder X-ray diffraction (PXRD) of GQDs@PCN-222 before and after photocatalysis showed that the photocatalyst still retained its original structure after photocatalysis (Figure S7).

$$\text{GQDs@PCN-222} \xrightarrow{h\nu} e^-(\text{GQDs}) + h^+(\text{PCN-222}) \quad (1)$$

$$2e^-(\text{GQDs}) + CO_2 + 2H^+ \rightarrow CO + H_2O \quad (2)$$

$$h^+(\text{PCN-222}) + \text{TEOA} \rightarrow \text{PCN-222} + \text{TEOA}^+ \quad (3)$$

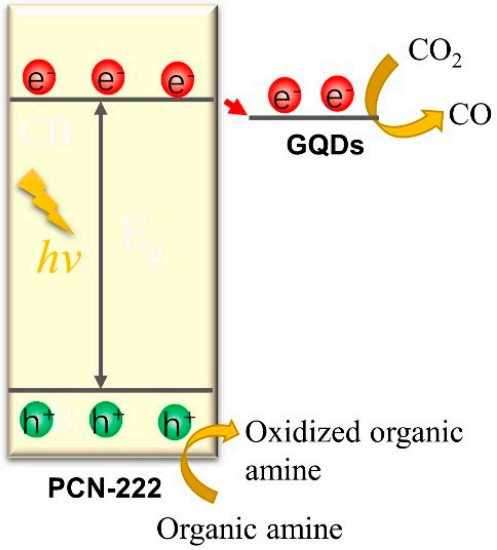


Figure 5. Proposed photocatalytic mechanism of CO_2 reduction to CO by GQDs@PCN-222.

3. Materials and Methods

3.1. Chemical Regents

High-purity graphite electrodes (99.9995%, metal basis, Alfa Aesar, Heysham, Britain), *N*,*N*-diethylformamide (DEF, 99%, Adamas, Shanghai, China), Zirconium(IV) Chloride ($ZrCl_4$, 98%, Adamas, Shanghai, China), Meso-tetra(4-carboxyphenyl)porphine (H_2TCPP, 98%, TCI, Tokyo, Japan), Benzoic acid (99%, Adamas, Shanghai, China), *N*,*N*-Dimethylformamide (DMF, 99.5%, Adamas, Shanghai, China), Hydrochloric Acid (HCl, 4 M, 37%, Adamas, Shanghai, China) acetone (99.5%, Adamas, Shanghai, China), Sodium Sulfate (Na_2SO_4, 99%, Greagent, Shanghai, China), Ethanol (99.5%, Adamas, Shanghai, China), Nafion 'D-521 dispersion, 5% *w*/*w* in water and 1-propanol (Alfa Aesar, Heysham, Britain), Triethanolamine (TEOA, 97%, Merk, Darmstadt, Germany), Diethyl ether (99.7%, Greagent, Shanghai, China).

3.2. The Synthesis of Graphene Quantum Dots (GQDs)

A total of 500 mL of deionized water was added into a volume of 800 mL beaker and then two high-purity graphite electrodes were put into the above beaker. In the beaker, the distance between two electrodes was set to 7 cm, and the potential was set to 30 V DC. After electrolysis of the two high-purity graphite electrodes for two weeks, the clear and colorless pure water gradually turned black. The black electrolyte was then centrifuged for one hour with a speed of 20,000 rpm, and the supernatant was then evaporated to obtain the required GQDs.

3.3. Preparation of GQDs Dispersion

A total of 25 mg of GQDs were dispersed into 5 mL of *N*,*N*-diethylformamide (DEF), resulting in 5 mg/mL of GQDs dispersion.

3.4. Synthesis of PCN-222

For the synthesis of PCN-222, a mixture of $ZrCl_4$ (70 mg), meso-tetra(4-carboxyphenyl) porphine (H_2TCPP, 50 mg), and benzoic acid (2700 mg) was ultrasonically dissolved in 8 mL of DEF in a volume of 20 mL Teflon-lined bomb. The mixture was heated in a 120 °C oven for 48 h and then a 130 °C oven for 24 h. After cooling down to room temperature, the sample was collected by centrifugation and washed with DMF three times. To further activate the sample, the obtained PCN-222 was suspended in a solution of 1.5 mL of 4 M HCl in 100 mL of DMF. Then, the mixture was heated in a 120 °C oven for 12 h. The sample was then centrifuged and washed with acetone three times. Finally, the sample was dried in a vacuum overnight at 80 °C, and about 60 mg of PCN-222 was obtained.

3.5. Synthesis of GQDs@PCN-222

For the synthesis of the GQDs@PCN-222, a mixture of $ZrCl_4$ (70 mg), H_2TCPP (50 mg), and benzoic acid (2700 mg) was ultrasonically dissolved in 8 mL of DEF in a 20 mL volume of Teflon-lined bomb. Then, 0.24 mL of GQDs dispersion (5 mg/mL) was added. The mixture was heated in a 120 °C oven for 48 h and then a 130 °C oven for 24 h. After cooling down to room temperature, the sample was collected by centrifugation and washed with DMF three times. To further activate the sample, the obtained PCN-222 was suspended in a solution of 1.5 mL of 4 M HCl in 100 mL of DMF. Then, the mixture was heated in a 120 °C oven for 12 h. The sample was then centrifuged and washed with acetone three times. Lastly, the sample was dried in a vacuum overnight at 80 °C.

3.6. Characterizations

The powder X-ray diffraction (PXRD) measurements were recorded on a powder X-ray diffractometer (MiniFlex 600, Rigaku Corporation, Tokyo, Japan) with Cu Ka radiation. X-ray photoelectron spectroscopy (XPS) data were acquired from a Thermo Fisher Scientific K-Alpha electron spectrometer (ESCALAB 250Xi, Thermo Fisher Scientific, Waltham, MA, USA). The morphologies of the samples were characterized by the scanning electron microscopy (SEM, JSM6700-F, JEOL, Akishima, Japan) and high-resolution transmission electron microscopy (HRTEM, Tecnai F20, FEI, Hillsboro, OR, USA). The specific surface areas were measured by Brunauer–Emmett–Teller (BET) on a Micrometrics ASAP 2020 system (ASAP 2020, Micrometrics Instrument Corp., Norcross, GA, USA). The samples were degassed at 120 °C for 2 h before the measurement and the N_2 sorption isotherms were obtained at 77 K. The PL emission spectra were recorded on a Horiba FluoroLog-3 spectrometer (FluoroLog-3, Horiba, Ltd., Kyoto, Japan). The solid UV-Vis absorption spectra were conducted using a UV–Vis spectrophotometer (UH4150, Hitachi, Tokyo, Japan).

3.7. Photoelectrochemical Measurements

The photoelectrochemical measurements were conducted at a Zahner Zennium electrochemical workstation (Zennium, Zahner scientific instruments, Gundelsdorf, Germany) by a typical three-electrode system in 0.5 M Na_2SO_4. A graphite rod was used as a counter electrode, while an Ag/AgCl electrode was used as a reference electrode. The working electrode was prepared as follows, 5 mg of the catalyst was dispersed in 1 mL of ethanol for 1 h, and then 30 μL of Nafion (5 wt%) was added to the mixture, followed by ultrasonic dispersion for 20 min. Then, drop the obtained catalyst liquid onto the FTO, cover the electrode of 1 cm^2, and dry for 2 h. Then, transient photocurrent plots and Mott-Schottky plots were obtained. Notably, the transient photocurrent plots were obtained under the same condition as photocatalytic CO_2 reduction.

3.8. Photocatalytic Reduction of CO_2

The photoreduction of CO_2 by photocatalysts was conducted under visible light irradiation. In a typical procedure, 10 mg of photocatalysts were evenly dispersed on the quartz filter membrane, which had been placed in the solid-gas photocatalytic reaction device. Then, 2 mL of a mixture of acetonitrile and triethanolamine (the volume ratio of acetonitrile to TEOA is 4:1) was dropped on the sample. Afterwards, the system was degassed and filled with CO_2 three times, making sure that all the air in the system was replaced by CO_2. The system was kept at a dark condition for 1 h and then irradiated by 300 W Xe light with a 420 nm cutter to start the photoreduction reaction. The produced gas in the system was analyzed by a Gas Chromatography (GC7890, Agilent Technologies Co., Ltd., Santa Clara, CA, USA) with TCD and FID detector every 2 h.

4. Conclusions

In summary, GQDs had been in situ encapsulated into a highly stable porphyrin MOF, PCN-222, by the solvothermal method. The linker, deep purple porphyrins, makes GQDs@PCN-222 a highly visible light harvester up to 800 nm. After incorporation of GQDs, the shape of GQDs@PCN-222 particles remained, revealed by SEM. The crystallized and porous structure of obtained GQDs@PCN-222 also remained. As most of the GQDs were covered by thick PCN-222, it was hard to observe those GQDs using HRTEM directly, the treatment of digested GQDs@PCN-222 rods by immersion in a 1 mm aqueous KOH solution can make the incorporated GQDs visible in HRTEM. The GQDs@PCN-222 could combine the advantages of MOFs and GQDs, overcome the disadvantage of low catalytic activity of pure MOFs, and be used for high-efficiency photocatalytic CO_2 reduction. Compared with PCN-222, the increased photocurrent and decreased PL emission of GQDs@PCN-222 indicated that the introduction of GQDs improves the separation efficiency and decreases the recombination of photogenerated electron–hole pairs of the catalyst, and then improves the visible light photocatalytic carbon dioxide reduction activity. Thus, the activity of GQDs@PCN-222 was almost four times higher than that of pure PCN-222, reaching 147.8 μmol/g/h in a 10 h period under visible light irradiation. This study demonstrated that the combination of GQDs and high light absorption MOFs provides a new platform for photocatalytic CO_2 reduction.

Supplementary Materials: The following supporting information can be downloaded at: https://www.mdpi.com/article/10.3390/molecules28124703/s1, References [38,47,51,53,61–67] are cited in the Supplementary Materials. Figure S1. Pore size distribution of PCN-222 and GQDs@PCN-222; Figure S2: SEM images of PCN-222; Figure S3: TEM and HRTEM images of GQDs/PCN-222; Figure S4: Solid UV-Vis diffuse reflectance spectrum and Tauc plot of H_2TCPP; Figure S5: Solid UV-Vis diffuse reflectance spectrum (a) and Tauc plot (b) of PCN-222; Figure S6: Mott-Schottky plots of PCN-222 with a frequency of 500, 1000, and 1500 HZ; Figure S7: PXRD patterns of GQDs@PCN-222 before and after photocatalysis; Table S1: Comparison of photocatalysts for CO_2 reduction with previous works.

Author Contributions: Conceptualization, Q.Y. and X.W.; methodology, Q.Y.; software, Q.Y.; validation, Q.Y., X.W., W.W., X.F., D.K., X.R. and U.K.; formal analysis, Q.Y., X.W., W.W., X.F., D.K., X.R., L.L. and U.K.; investigation, Q.Y., X.W., W.W., X.F., D.K., X.R. and U.K.; resources, X.W.; data curation, Q.Y. and X.W.; writing—original draft preparation, Q.Y. and X.W.; writing—review and editing, Q.Y., X.W., W.W., X.F., D.K., X.R., L.L. and U.K.; visualization, Q.Y., X.W., W.W., X.F., D.K., X.R. and U.K.; supervision, X.W.; project administration, X.W.; funding acquisition, X.W. All authors have read and agreed to the published version of the manuscript.

Funding: We are grateful for the financial support from the Guangdong Basic and Applied Basic Research Foundation (No. 2020A1515110003), the National Natural Science Foundation of China (No. 22001094), research funds of Zhejiang Sci-Tech University (No. 21212302-Y, 21212302-Y), and the open fund of Guangdong Provincial Key Laboratory of Functional Supramolecular Coordination Materials and Applications (No. 2022A06).

Institutional Review Board Statement: Not applicable.

Informed Consent Statement: Not applicable.

Data Availability Statement: Not applicable.

Conflicts of Interest: The authors declare no conflict of interest.

Sample Availability: Not applicable.

References

1. Dahl, T.W.; Harding, M.A.R.; Brugger, J.; Feulner, G.; Norrman, K.; Lomax, B.H.; Junium, C.K. Low atmospheric CO_2 levels before the rise of forested ecosystems. *Nat. Commun.* **2022**, *13*, 7616. [CrossRef]
2. Xu, A.; Hung, S.-F.; Cao, A.; Wang, Z.; Karmodak, N.; Huang, J.E.; Yan, Y.; Sedighian Rasouli, A.; Ozden, A.; Wu, F.-Y.; et al. Copper/alkaline earth metal oxide interfaces for electrochemical CO_2-to-alcohol conversion by selective hydrogenation. *Nat. Catal.* **2022**, *5*, 1081–1088. [CrossRef]
3. Bhattacharjee, S.; Rahaman, M.; Andrei, V.; Miller, M.; Rodríguez-Jiménez, S.; Lam, E.; Pornrungroj, C.; Reisner, E. Photoelectrochemical CO_2-to-fuel conversion with simultaneous plastic reforming. *Nat. Synth.* **2023**, *2*, 182–192. [CrossRef]
4. Ye, R.; Wang, X.; Wang, G.; Chen, Y.; Lai, Q.; Zhang, R. Editorial: Heterogeneous catalysts for C1 molecules conversion. *Front. Chem.* **2022**, *10*, 1121871. [CrossRef] [PubMed]
5. Yang, G.; Li, Y.; Wang, Q.; Wang, X.; Zuo, S.; Zhang, H.; Ren, X.; He, Y.; Ichihara, F.; Ye, J. Synergy between Confined Cobalt Centers and Oxygen Defects on α-Fe_2O_3 Platelets for Efficient Photocatalytic CO_2 Reduction. *Sol. RRL* **2022**, *6*, 2100833. [CrossRef]
6. Xu, R.; Si, D.H.; Zhao, S.S.; Wu, Q.J.; Wang, X.S.; Liu, T.F.; Zhao, H.; Cao, R.; Huang, Y.B. Tandem Photocatalysis of CO_2 to C_2H_4 via a Synergistic Rhenium-(I) Bipyridine/Copper-Porphyrinic Triazine Framework. *J. Am. Chem. Soc.* **2023**, *145*, 8261–8270. [CrossRef] [PubMed]
7. Zheng, K.; Wu, Y.; Hu, Z.; Wang, S.; Jiao, X.; Zhu, J.; Sun, Y.; Xie, Y. Progress and perspective for conversion of plastic wastes into valuable chemicals. *Chem. Soc. Rev.* **2023**, *52*, 8–29. [CrossRef]
8. Xiong, Q.; Chen, Y.; Xu, T.; Zhu, Z.; Chen, W.; Lu, W. Highly efficient purification of emerging pollutants and bacteria in natural water by g-C_3N_4-sheltered fibers containing TiO_2. *Appl. Surf. Sci.* **2021**, *559*, 149839. [CrossRef]
9. Wang, T.; Dai, Z.; Kang, J.; Fu, F.; Zhang, T.; Wang, S. A TiO_2 nanocomposite hydrogel for hydroponic plants in efficient water improvement. *Mater. Chem. Phys.* **2018**, *215*, 242–250. [CrossRef]
10. Sun, Y.; Luo, Y.; Zhu, Y.; Fu, Y. Improved visible-light photocatalytic activity of sodium tantalum oxide via biomass-derived silk fibroin doping. *Text. Res. J.* **2018**, *89*, 1332–1339. [CrossRef]
11. Jiang, T.; Jiang, G.; Li, L.; Chen, H.; Zhou, H.; Yao, J.; Kong, X.; Chen, W. N-Doped carbon hybrid conjugates as vectors for photocatalytic CS_2 production. *Mater. Res. Express* **2015**, *2*, 045603. [CrossRef]
12. Liu, B.; Xu, Y.; Cui, J.; Wang, S.; Wang, T. Carbon nanotubes-dispersed TiO_2 nanoparticles with their enhanced photocatalytic activity. *Mater. Res. Bull.* **2014**, *59*, 278–282. [CrossRef]
13. Liu, C.; Qian, X.; Wei, Q.; Chen, Z.; Chen, J.; Wang, W.; Chen, X.; Gao, J.; Liu, Y.; Xie, L. Construction of hydrostable cesium lead bromide-titania for visible-light degradation of tetracycline hydrochloride in water. *J. Clean. Prod.* **2022**, *365*, 132830. [CrossRef]
14. Gao, J.; Qian, X.; Wei, Q.; Chen, Z.; Liu, C.; Wang, W.; Chen, J.; Chen, X.; Liu, Y.; Wei, G. Construction of core-shell cesium lead bromide-silica by precipitation coating method with applications in aqueous photocatalysis. *J. Colloid Interface Sci.* **2022**, *623*, 974–984. [CrossRef]
15. Yang, X.; Chen, Z.; Zhao, W.; Liu, C.; Qian, X.; Zhang, M.; Wei, G.; Khan, E.; Hau Ng, Y.; Sik Ok, Y. Recent advances in photodegradation of antibiotic residues in water. *Chem. Eng. J.* **2021**, *405*, 126806. [CrossRef]
16. Chandel, M.; Thakur, M.; Sharma, A.; Pathania, D.; Kumar, A.; Singh, L. Chlorophyll sensitized $(BiO)_2CO_3$/ $CdWO_4$/rGO nano-hybrid assembly for solar assisted photo-degradation of chlorzoxazone. *Chemosphere* **2022**, *305*, 135472. [CrossRef]
17. Kumar, A.; Sharma, K.; Thakur, M.; Pathania, D.; Sharma, A. Fabrication of high visible light active $LaFeO_3$/Cl-g-C_3N_4/RGO heterojunction for solar assisted photo-degradation of aceclofenac. *J. Environ. Chem. Eng.* **2022**, *10*, 108098. [CrossRef]
18. Li, D.; Kassymova, M.; Cai, X.; Zang, S.-Q.; Jiang, H.-L. Photocatalytic CO_2 reduction over metal-organic framework-based materials. *Coord. Chem. Rev.* **2020**, *412*, 213262. [CrossRef]
19. Li, L.; Wang, X.S.; Liu, T.F.; Ye, J. Titanium-based MOF materials: From crystal engineering to photocatalysis. *Small Methods* **2020**, *4*, 2000486. [CrossRef]
20. Wang, X.S.; Li, L.; Li, D.; Ye, J. Recent progress on exploring stable metal–organic frameworks for photocatalytic solar fuel production. *Sol. RRL* **2020**, *4*, 1900547. [CrossRef]
21. Lei, Q.; Yuan, H.; Du, J.; Ming, M.; Yang, S.; Chen, Y.; Lei, J.; Han, Z. Photocatalytic CO_2 reduction with aminoanthraquinone organic dyes. *Nat. Commun.* **2023**, *14*, 1087. [CrossRef] [PubMed]
22. Li, H.; Cheng, C.; Yang, Z.; Wei, J. Encapsulated CdSe/CdS nanorods in double-shelled porous nanocomposites for efficient photocatalytic CO_2 reduction. *Nat. Commun.* **2022**, *13*, 6466. [CrossRef]
23. Zhou, J.; Li, J.; Kan, L.; Zhang, L.; Huang, Q.; Yan, Y.; Chen, Y.; Liu, J.; Li, S.L.; Lan, Y.Q. Linking oxidative and reductive clusters to prepare crystalline porous catalysts for photocatalytic CO_2 reduction with H_2O. *Nat. Commun.* **2022**, *13*, 4681. [CrossRef]
24. Lv, J.; Xie, J.; Mohamed, A.G.A.; Zhang, X.; Feng, Y.; Jiao, L.; Zhou, E.; Yuan, D.; Wang, Y. Solar utilization beyond photosynthesis. *Nat. Rev. Chem.* **2022**, *7*, 91–105. [CrossRef]

25. Zhao, Y.; Zeng, H.; Zhu, X.W.; Lu, W.; Li, D. Metal-organic frameworks as photoluminescent biosensing platforms: Mechanisms and applications. *Chem. Soc. Rev.* **2021**, *50*, 4484–4513. [CrossRef]
26. Li, L.; Fang, Z.-B.; Deng, W.; Yi, J.-D.; Wang, R.; Liu, T.-F. Precise Construction of Stable Bimetallic Metal–Organic Frameworks with Single-Site Ti(IV) Incorporation in Nodes for Efficient Photocatalytic Oxygen Evolution. *CCS Chem.* **2022**, *4*, 2782–2792. [CrossRef]
27. Datta, S.J.; Mayoral, A.; Murthy Srivatsa Bettahalli, N.; Bhatt, P.M.; Karunakaran, M.; Carja, I.D.; Fan, D.; Graziane, M.M.P.; Semino, R.; Maurin, G.; et al. Rational design of mixed-matrix metal-organic framework membranes for molecular separations. *Science* **2022**, *376*, 1080–1087. [CrossRef] [PubMed]
28. Fonseca, J.; Meng, L.; Imaz, I.; Maspoch, D. Self-assembly of colloidal metal-organic framework (MOF) particles. *Chem. Soc. Rev.* **2023**, *52*, 2528–2543. [CrossRef]
29. Hu, N.; Cai, Y.; Li, L.; Wang, X.; Gao, J. Amino-functionalized titanium based metal-organic framework for photocatalytic hydrogen production. *Molecules* **2022**, *27*, 4241. [CrossRef] [PubMed]
30. Fan, L.; Yu, Q.; Chen, J.; Khan, U.; Wang, X.; Gao, J. Achievements and perspectives in metal–organic framework-based materials for photocatalytic nitrogen reduction. *Catalysts* **2022**, *12*, 1005. [CrossRef]
31. Navalon, S.; Dhakshinamoorthy, A.; Alvaro, M.; Ferrer, B.; Garcia, H. Metal-Organic Frameworks as Photocatalysts for Solar-Driven Overall Water Splitting. *Chem. Rev.* **2023**, *123*, 445–490. [CrossRef]
32. Zhang, J.; Huang, J.; Wang, L.; Sun, P.; Wang, P.; Yao, Z.; Yang, Y. Coupling bimetallic NiMn-MOF nanosheets on $NiCo_2O_4$ nanowire arrays with boosted electrochemical performance for hybrid supercapacitor. *Mater. Res. Bull.* **2022**, *149*, 111707. [CrossRef]
33. Yu, Z.; Kang, S.; Wang, J.; Tai, M.; Wang, X.; Ding, Y.; Jin, D.; Wang, L. Highly improved photoluminescence properties of novel ternary Eu(cpioa)phen metal–organic frameworks. *Funct. Mater. Lett.* **2022**, *15*, 2251026. [CrossRef]
34. Sun, P.; Zhang, J.; Huang, J.; Wang, L.; Wang, P.; Cai, C.; Lu, M.; Yao, Z.; Yang, Y. Bimetallic MOF-derived (CuCo)Se nanoparticles embedded in nitrogen-doped carbon framework with boosted electrochemical performance for hybrid supercapacitor. *Mater. Res. Bull.* **2021**, *137*, 111196. [CrossRef]
35. Lei, Z.; Tang, Q.; Ju, Y.; Lin, Y.; Bai, X.; Luo, H.; Tong, Z. Block copolymer@ZIF-8 nanocomposites as a pH-responsive multi-steps release system for controlled drug delivery. *J. Biomater. Sci. Polym. Ed.* **2020**, *31*, 695–711. [CrossRef]
36. Li, G.; Cai, H.; Li, X.; Zhang, J.; Zhang, D.; Yang, Y.; Xiong, J. Construction of hierarchical $NiCo_2O_4$@Ni-MOF hybrid arrays on carbon cloth as superior battery-type electrodes for flexible solid-state hybrid supercapacitors. *ACS Appl. Mater. Interfaces* **2019**, *11*, 37675–37684. [CrossRef]
37. He, H.; Wang, X.; Yu, Q.; Wu, W.; Feng, X.; Kong, D.; Ren, X.; Gao, J. In Situ Growth of Ti_3C_2/UiO-66-NH_2 Composites for Photoreduction of Cr(VI). *Catalysts* **2023**, *13*, 876. [CrossRef]
38. Wang, X.; Yang, X.; Chen, C.; Li, H.; Huang, Y.; Cao, R. Graphene quantum dots supported on Fe-based metal-organic frameworks for efficient photocatalytic CO_2 reduction. *Acta Chim. Sin.* **2022**, *80*, 22–28. [CrossRef]
39. Lin, J.B.; Nguyen, T.T.T.; Vaidhyanathan, R.; Burner, J.; Taylor, J.M.; Durekova, H.; Akhtar, F.; Mah, R.K.; Ghaffari-Nik, O.; Marx, S.; et al. A scalable metal-organic framework as a durable physisorbent for carbon dioxide capture. *Science* **2021**, *374*, 1464–1469. [CrossRef] [PubMed]
40. Li, N.; Liu, J.; Liu, J.J.; Dong, L.Z.; Xin, Z.F.; Teng, Y.L.; Lan, Y.Q. Adenine Components in Biomimetic Metal-Organic Frameworks for Efficient CO_2 Photoconversion. *Angew. Chem. Int. Ed.* **2019**, *58*, 5226–5231. [CrossRef]
41. Chen, E.X.; Qiu, M.; Zhang, Y.F.; He, L.; Sun, Y.Y.; Zheng, H.L.; Wu, X.; Zhang, J.; Lin, Q. Energy Band Alignment and Redox-Active Sites in Metalloporphyrin-Spaced Metal-Catechol Frameworks for Enhanced CO_2 Photoreduction. *Angew. Chem. Int. Ed.* **2022**, *61*, e202111622.
42. Jiang, Z.; Xu, X.; Ma, Y.; Cho, H.S.; Ding, D.; Wang, C.; Wu, J.; Oleynikov, P.; Jia, M.; Cheng, J.; et al. Filling Metal-Organic Framework Mesopores with TiO_2 for CO_2 Photoreduction. *Nature* **2020**, *586*, 549–554. [CrossRef]
43. Liu, J.; Fan, Y.-Z.; Li, X.; Wei, Z.; Xu, Y.-W.; Zhang, L.; Su, C.-Y. A porous rhodium(III)-porphyrin metal-organic framework as an efficient and selective photocatalyst for CO_2 reduction. *Appl. Catal. B Environ.* **2018**, *231*, 173–181. [CrossRef]
44. Yan, Z.H.; Du, M.H.; Liu, J.; Jin, S.; Wang, C.; Zhuang, G.L.; Kong, X.J.; Long, L.S.; Zheng, L.S. Photo-generated dinuclear $\{Eu(II)\}_2$ active sites for selective CO_2 reduction in a photosensitizing metal-organic framework. *Nat. Commun.* **2018**, *9*, 3353. [CrossRef] [PubMed]
45. Dong, L.Z.; Zhang, L.; Liu, J.; Huang, Q.; Lu, M.; Ji, W.X.; Lan, Y.Q. Stable Heterometallic Cluster-Based Organic Framework Catalysts for Artificial Photosynthesis. *Angew. Chem. Int. Ed.* **2020**, *59*, 2659–2663. [CrossRef] [PubMed]
46. Jiang, Y.; Yu, Y.; Zhang, X.; Weinert, M.; Song, X.; Ai, J.; Han, L.; Fei, H. N-Heterocyclic Carbene-Stabilized Ultrasmall Gold Nanoclusters in a Metal-Organic Framework for Photocatalytic CO_2 Reduction. *Angew. Chem. Int. Ed.* **2021**, *60*, 17388–17393. [CrossRef] [PubMed]
47. Fu, Y.; Sun, D.; Chen, Y.; Huang, R.; Ding, Z.; Fu, X.; Li, Z. An amine-functionalized titanium metal-organic framework photocatalyst with visible-light-induced activity for CO_2 reduction. *Angew. Chem. Int. Ed.* **2012**, *51*, 3364–3367. [CrossRef]
48. Xu, H.Q.; Hu, J.; Wang, D.; Li, Z.; Zhang, Q.; Luo, Y.; Yu, S.H.; Jiang, H.L. Visible-Light Photoreduction of CO_2 in a Metal-Organic Framework: Boosting Electron-Hole Separation via Electron Trap States. *J. Am. Chem. Soc.* **2015**, *137*, 13440–13443. [CrossRef]
49. Wang, X.; Zhao, X.; Zhang, D.; Li, G.; Li, H. Microwave irradiation induced UIO-66-NH_2 anchored on graphene with high activity for photocatalytic reduction of CO_2. *Appl. Catal. B Environ.* **2018**, *228*, 47–53. [CrossRef]

50. Choi, K.M.; Kim, D.; Rungtaweevoranit, B.; Trickett, C.A.; Barmanbek, J.T.; Alshammari, A.S.; Yang, P.; Yaghi, O.M. Plasmon-Enhanced Photocatalytic CO_2 Conversion within Metal-Organic Frameworks under Visible Light. *J. Am. Chem. Soc.* **2017**, *139*, 356–362. [CrossRef]
51. Shi, L.; Wang, T.; Zhang, H.; Chang, K.; Ye, J. Electrostatic Self-Assembly of Nanosized Carbon Nitride Nanosheet onto a Zirconium Metal-Organic Framework for Enhanced Photocatalytic CO_2 Reduction. *Adv. Funct. Mater.* **2015**, *25*, 5360–5367. [CrossRef]
52. Sun, D.; Liu, W.; Fu, Y.; Fang, Z.; Sun, F.; Fu, X.; Zhang, Y.; Li, Z. Noble metals can have different effects on photocatalysis over metal-organic frameworks (MOFs): A case study on M/NH_2-MIL-125(Ti) (M=Pt and Au). *Chem. Eur. J.* **2014**, *20*, 4780–4788. [CrossRef] [PubMed]
53. Zhao, H.; Wang, X.; Feng, J.; Chen, Y.; Yang, X.; Gao, S.; Cao, R. Synthesis and characterization of Zn_2GeO_4/Mg-MOF-74 composites with enhanced photocatalytic activity for CO_2 reduction. *Catal. Sci. Technol.* **2018**, *8*, 1288–1295. [CrossRef]
54. Zhang, Z.; Zhang, J.; Chen, N.; Qu, L. Graphene quantum dots: An emerging material for energy-related applications and beyond. *Energy Environ. Sci.* **2012**, *5*, 8869. [CrossRef]
55. Liu, J.; Liu, Y.; Liu, N.; Han, Y.; Zhang, X.; Huang, H.; Lifshitz, Y.; Lee, S.T.; Zhong, J.; Kang, Z. Metal-free efficient photocatalyst for stable visible water splitting via a two-electron pathway. *Science* **2015**, *347*, 970–974. [CrossRef]
56. Ming, H.; Ma, Z.; Liu, Y.; Pan, K.; Yu, H.; Wang, F.; Kang, Z. Large scale electrochemical synthesis of high quality carbon nanodots and their photocatalytic property. *Dalton Trans.* **2012**, *41*, 9526–9531. [CrossRef]
57. Thommes, M.; Kaneko, K.; Neimark, A.V.; Olivier, J.P.; Rodriguez-Reinoso, F.; Rouquerol, J.; Sing, K.S.W. Physisorption of gases, with special reference to the evaluation of surface area and pore size distribution (IUPAC Technical Report). *Pure Appl. Chem.* **2015**, *87*, 1051–1069. [CrossRef]
58. Gu, Z.G.; Li, D.J.; Zheng, C.; Kang, Y.; Woll, C.; Zhang, J. MOF-Templated Synthesis of Ultrasmall Photoluminescent Carbon-Nanodot Arrays for Optical Applications. *Angew. Chem. Int. Ed.* **2017**, *56*, 6853–6858. [CrossRef]
59. Wang, X.-S.; Chen, C.-H.; Ichihara, F.; Oshikiri, M.; Liang, J.; Li, L.; Li, Y.; Song, H.; Wang, S.; Zhang, T.; et al. Integration of adsorption and photosensitivity capabilities into a cationic multivariate metal-organic framework for enhanced visible-light photoreduction reaction. *Appl. Catal. B Environ.* **2019**, *253*, 323–330. [CrossRef]
60. Huang, H.; Wang, X.-S.; Philo, D.; Ichihara, F.; Song, H.; Li, Y.; Li, D.; Qiu, T.; Wang, S.; Ye, J. Toward visible-light-assisted photocatalytic nitrogen fixation: A titanium metal organic framework with functionalized ligands. *Appl. Catal. B Environ.* **2020**, *267*, 118686. [CrossRef]
61. Chen, E.X.; Qiu, M.; Zhang, Y.F.; Zhu, Y.S.; Liu, L.Y.; Sun, Y.Y.; Bu, X.; Zhang, J.; Lin, Q. Acid and Base Resistant Zirconium Polyphenolate-Metalloporphyrin Scaffolds for Efficient CO_2 Photoreduction. *Adv. Mater.* **2018**, *30*, 1704388. [CrossRef] [PubMed]
62. Zhang, H.; Wei, J.; Dong, J.; Liu, G.; Shi, L.; An, P.; Zhao, G.; Kong, J.; Wang, X.; Meng, X.; et al. Efficient Visible-Light-Driven Carbon Dioxide Reduction by a Single-Atom Implanted Metal-Organic Framework. *Angew. Chem. Int. Ed.* **2016**, *55*, 14310–14314. [CrossRef] [PubMed]
63. Huang, Q.; Liu, J.; Feng, L.; Wang, Q.; Guan, W.; Dong, L.Z.; Zhang, L.; Yan, L.K.; Lan, Y.Q.; Zhou, H.C. Multielectron transportation of polyoxometalate-grafted metalloporphyrin coordination frameworks for selective CO_2-to-CH_4 photoconversion. *Natl. Sci. Rev.* **2020**, *7*, 53–63. [CrossRef] [PubMed]
64. Xie, Y.; Fang, Z.; Li, L.; Yang, H.; Liu, T.F. Creating Chemisorption Sites for Enhanced CO_2 Photoreduction Activity through Alkylamine Modification of MIL-101-Cr. *ACS Appl. Mater. Interfaces* **2019**, *11*, 27017–27023. [CrossRef] [PubMed]
65. Kong, Z.-C.; Liao, J.-F.; Dong, Y.-J.; Xu, Y.-F.; Chen, H.-Y.; Kuang, D.-B.; Su, C.-Y. Core@Shell CsPbBr3@Zeolitic Imidazolate Framework Nanocomposite for Efficient Photocatalytic CO_2 Reduction. *ACS Energy Lett.* **2018**, *3*, 2656–2662. [CrossRef]
66. Li, M.; Wang, M.; Zhu, L.; Li, Y.; Yan, Z.; Shen, Z.; Cao, X. Facile microwave assisted synthesis of N-rich carbon quantum dots/dual-phase TiO_2 heterostructured nanocomposites with high activity in CO_2 photoreduction. *Appl. Catal. B Environ.* **2018**, *231*, 269–276. [CrossRef]
67. Li, H.; Deng, Y.; Liu, Y.; Zeng, X.; Wiley, D.; Huang, J. Carbon quantum dots and carbon layer double protected cuprous oxide for efficient visible light CO_2 reduction. *Chem. Commun.* **2019**, *55*, 4419–4422. [CrossRef]

Disclaimer/Publisher's Note: The statements, opinions and data contained in all publications are solely those of the individual author(s) and contributor(s) and not of MDPI and/or the editor(s). MDPI and/or the editor(s) disclaim responsibility for any injury to people or property resulting from any ideas, methods, instructions or products referred to in the content.